Article

Coupling Amorphization and Compositional Optimization of Ternary Metal Phosphides toward High-Performance Electrocatalytic Hydrogen Production

Bing Deng,*,[§§] Zhen-Yu Wu,[§§] Erkang Feng, Lu Ma, Zhe Wang, Jinhang Chen, Lucas Eddy, Alexander Lathem, Teng Wang, Weiyin Chen, Yi Cheng, Shichen Xu, Qiming Liu, Boris I. Yakobson, Haotian Wang,* Yufeng Zhao,* and James M. Tour*

Cite This: https://doi.org/10.1021/jacs.5c00071

Read Online

ACCESS | ⬛ Metrics & More | 📰 Article Recommendations | 🆂🆘 Supporting Information

ABSTRACT: Amorphous materials, with abundant active sites and unique electronic configurations, have the potential to outperform their crystalline counterparts in high-performance catalysis for clean energy. However, their synthesis and compositional optimization remain underexplored due to the strict conditions required for their formation. Here, we report the synthesis of ternary platinum-nickel-phosphorus (PtNiP) amorphous nanoparticles (ANPs) within milliseconds by flash Joule heating, which features ultrafast cooling that enables the vitrification of metal precursors. Through compositional optimization, the Gibbs free energy of hydrogen adsorption for $Pt_4Ni_4P_1$ ANPs is optimized at 0.02 eV, an almost ideal value, even surpassing that of the benchmark metallic platinum catalyst. As a result, the PtNiP ANPs exhibited superior activity in electrocatalytic hydrogen evolution in acid electrolyte ($\eta_{10} \sim 14$ mV, Tafel slope ~ 18 mV dec^{-1}, and mass activity 5× higher than state-of-the-art Pt/C). Life-cycle assessment and technoeconomic analysis suggest that, compared to existing processes, our approach enables notable reductions in greenhouse gas emission, energy consumption, and production cost for practical electrolyzer catalyst manufacturing.
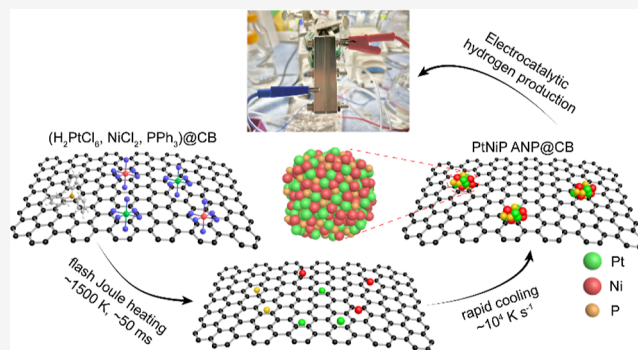
INTRODUCTION

Hydrogen (H_2) holds great promise as a clean, low-carbon energy carrier for achieving sustainability and decarbonization.[1,2] However, the high cost and scarcity of noble metals, such as platinum (Pt) and palladium (Pd), have limited their widespread use in fuel cells and electrolyzers.[1,3] Great efforts have been made to enhance noble metal utilization efficiency and to increase intrinsic catalytic activity. Some effective strategies have been developed, including engineering the nanostructure of noble metals, such as nanoparticles[4,5] or single atoms,[6,7] to reduce mass loading, and composition engineering by alloying with non-noble metals, as seen in Pt—Ni nanoparticle[8] and Pt—Co nanocatalysts.[9] Additionally, strain engineering[10] and electronic structure tuning[11] have been employed to regulate hydrogen adsorption/desorption energies, leading to higher intrinsic activity and reduced noble metal consumption.

Amorphization is emerging as a promising strategy in structure engineering.[12] The absence of long-range order endows amorphous nanomaterials with unconventional electronic structures.[13,14] Due to the largely increased number of active sites and the presence of effective dangling bonds,

amorphous materials can surpass their crystalline counterparts in catalytic activity by overcoming their inherent in-plane inertness.[15,16] Various amorphous materials, including metal nanostructures,[17,18] metallic glasses,[19−24] oxides,[25] sulfides,[26,27] chalcogenides,[28] and phosphides,[29] have been reported in a wide range of catalytic processes. Despite their potential, several obstacles hinder the widespread application of amorphous materials. First, their syntheses often involve wet chemistry techniques such as chemical reduction[30−33] or electrochemical methods,[34,35] which can lead to contamination by surfactants[33] that are detrimental to the catalytic performance. Second, the synthesizability of amorphous structures is highly sensitive to elemental composition,[36] where small changes in compositional ratios can significantly affect formation. This limits the exploration of amorphous materials

across a broad compositional range. Third, modeling the electronic structure of amorphous materials is particularly challenging due to their disordered atomic configurations,[37] complicating the mechanistic explanation of their catalytic properties.

To address these challenges, we herein employed flash Joule heating[38−40] for the synthesis of PtNiP amorphous nanoparticles (ANPs) with widely tunable compositions. Metal precursors loaded on a carbon substrate were subjected to millisecond current pulses, rapidly raising the temperature through direct Joule heating. This caused the alloy to melt, followed by ultrafast cooling ($>10^4$ K s^{-1}) through thermal radiation, resulting in vitrification into ANPs. The atomic and electronic structures of amorphous PtNiP were modeled using a combination of ab initio molecular dynamics (MD) simulations and density functional theory (DFT) calculations. By optimizing the composition at $Pt_4Ni_4P_1$, we achieved a Gibbs free energy of hydrogen adsorption of 0.02 eV, an almost ideal value, superior to that of the benchmark metallic platinum catalyst. As a result, PtNiP ANPs exhibited very high intrinsic activity for the electrocatalytic hydrogen evolution reaction (HER) ($\eta_{10} \sim 14$ mV, Tafel slope ~ 18 mV dec^{-1}, and mass activity 5× higher than state-of-the-art Pt/C). A proton exchange membrane electrolyzer using PtNiP ANPs as the HER catalysts was assembled and operated consistently for >100 h at industrially relevant current densities. Comparative life-cycle assessment (LCA) and technoeconomic analysis (TEA) showed a substantial reduction in greenhouse gas emissions, energy consumption, and production costs, underscoring the practical application potential and environmental benefits of our process.

METHODS

Materials. H_2PtCl_6 (≥37.5 wt % Pt basis, Millipore-Sigma), $NiCl_2$ (98 wt %, Sigma-Aldrich), and triphenylphosphine (PPh$_3$, 99 wt %, Acros Organics) were used as the precursors. Carbon black (Carbot, Vulcan XC72) was used as the conductive additives and supports. The metal precursors were loaded onto carbon black by wet impregnation. The precursors were dissolved in ethanol at 0.05 M. The loading of Pt was fixed at 10 wt % with respect to carbon black. Ni and P amounts were calculated according to the designed molar ratio. H_2PtCl_6 and $NiCl_2$ were mixed, and carbon black was added into the mixed solution, followed by bath sonication (Cole-Parmer Ultrasonic Cleaner) for 10 min to enhance the dispersion and drying in a vacuum desiccator overnight. Next, black powder was added to the PPh$_3$ solution, followed by sonication and drying.

FJH Synthesis. The FJH system is composed of a capacitor bank with a total capacitance of 60 mF, switches, and an RLC circuit to control the discharging with a characteristic time of 0.1 ms.[41] The precursor mixture was loaded into a quartz tube with an inner diameter of 4 mm. Graphite rods were used as electrodes on both sides of the quartz tube and connected to the FJH system. The resistance of the sample was controlled to ~1 Ω by compressing the two electrodes. The reaction was conducted inside a desiccator filled with argon gas to prevent oxidation. The capacitor bank, capable of reaching 400 V, was first charged by a direct current supply. The discharging was controlled by a relay with a programmable delay time. After the FJH reaction, the sample was rapidly cooled to room temperature by thermal radiation.

Characterization. X-ray diffraction (XRD) was conducted on a Rigaku SmartLab XRD instrument using Cu Kα radiation (λ = 1.5406 Å). SEM images were obtained using an FEI Quanta 400 ESEM field emission microscope operated at 5 kV. EDS was collected at 30 kV using the same system equipped with an EDS detector. X-ray photoemission spectroscopy (XPS) spectra were acquired on a PHI Quantera XPS system under a pressure of 5×10^{-9} Torr. Full XPS

spectra were acquired with a step size of 0.5 eV and a pass energy of 140 eV, and XPS fine spectra were acquired with a step size of 0.1 eV and a pass energy of 26 eV. All XPS spectra were calibrated by using the standard C 1s peak at 284.8 eV. BF-TEM, high-resolution TEM (HRTEM), and selected-area electron diffraction (SAED) were collected using a JEOL 2100 field emission gun transmission electron microscope operating at 200 kV. High-angle annular dark-field scanning transmission electron microscopy (HAADF-STEM) imaging and EDS mapping were carried out on a FEI Titan Themis3 system equipped with image and probe aberration corrections and an electron monochromator operating at 80 kV. The temperature was measured using an IR thermometer (Micro-Epsilon, 200−1500 °C).

X-ray Absorption Spectroscopy Measurement. XAS for the Pt L_3-edge and Ni K edge in the fluorescence mode was measured at beamline 7-BM (QAS) of the National Synchrotron Light Source II (NSLS-II) at Brookhaven National Laboratory. The energy range of the X-ray provided by this beamline was 4.7−31 keV. Its monochromator is equipped with a Si(111) channel-cut crystal and runs at continuous scan mode. Pt and Ni foils were measured during data collection for energy calibration. The XAS data, including X-ray absorption near edge structure (XANES) and extended X-ray absorption fine structure (EXAFS), were analyzed using Athena and Artemis from the Demeter software package.

Electrocatalytic HER Measurement. The binder solution was prepared by mixing 5 wt % Nafion solution (50 µL, Sigma-Aldrich) with H_2O/EtOH (1 mL, v/v = 1:1). The catalyst inks were prepared by dispersion of the PtNiP ANPs catalysts (2.0 mg) into a binder solution (1 mL) followed by ultrasonication for 2 h. The ink (20 µL) was then drop cast onto a rotating disc electrode (RDE) with a diameter of 5 mm (surface area ~ 0.196 cm^2, catalyst loading of ~0.20 mg cm^{-2}). The catalyst ink was completely dried overnight before the test. The electrochemical measurements were conducted by using a CHI 608D electrochemical workstation in a 0.5 M H_2SO_4 solution. The standard three-electrode setup was applied, where an Ag/AgCl reference electrode was used as the standard, the catalyst-loaded RDE as the working electrode, and a graphite rod as the counter electrode. Before measurement, the electrolyte was purged with N_2 for 30 min for N_2 saturation. Cyclic voltammetry (CV) at a scan rate of 50 mV s^{-1} was conducted for 10 cycles to stabilize the catalyst. Linear sweep voltammetry was carried out at a scan rate of 5 mV s^{-1}. PtNi CPNs catalyst was used as a comparison, and commercial Pt/C catalyst (20 wt % loading, Sigma-Aldrich) was used as the benchmark.

Mass Activity Measurement. The Pt contents in various catalysts were determined by inductively coupled plasma mass spectrometry (ICP−MS). The samples (PtNiP ANPs supported on carbon black, PtNi CNPs supported on carbon black, and commercial Pt/C) were digested by an aqua regia process. The ICP−MS was conducted using a PerkinElmer Nexion 300 ICP−MS system. The geometric polarization curves for PtNiP ANPs, PtNi CNPs, and commercial Pt/C were then normalized according to their Pt mass loadings.

Calculation of the ECSA. The electrochemically active surface area (ECSA) of the electrodes loaded with various catalysts was determined by C_{dl} measurement within a non-Faradaic potential range. The specific capacitance (C_s) for a flat surface is generally 20−60 µF cm^{-2},[7] and a value of $C_s = 40$ µF cm^{-2} is used in this work. The ECSA is determined by

$$ECSA = \frac{C_{dl}}{C_s} \tag{1}$$

The estimated ECSA values match well with those calculated from the particle size distribution.

Active Site Measurement by Cu Underpotential Deposition. The Cu underpotential deposition (UPD) has been an ideal method for determining the active sites of Pt-based catalysts.[4,42] In this method, the number of active sites (n) could be quantified by the Cu UPD stripping charges (Q_{Cu})
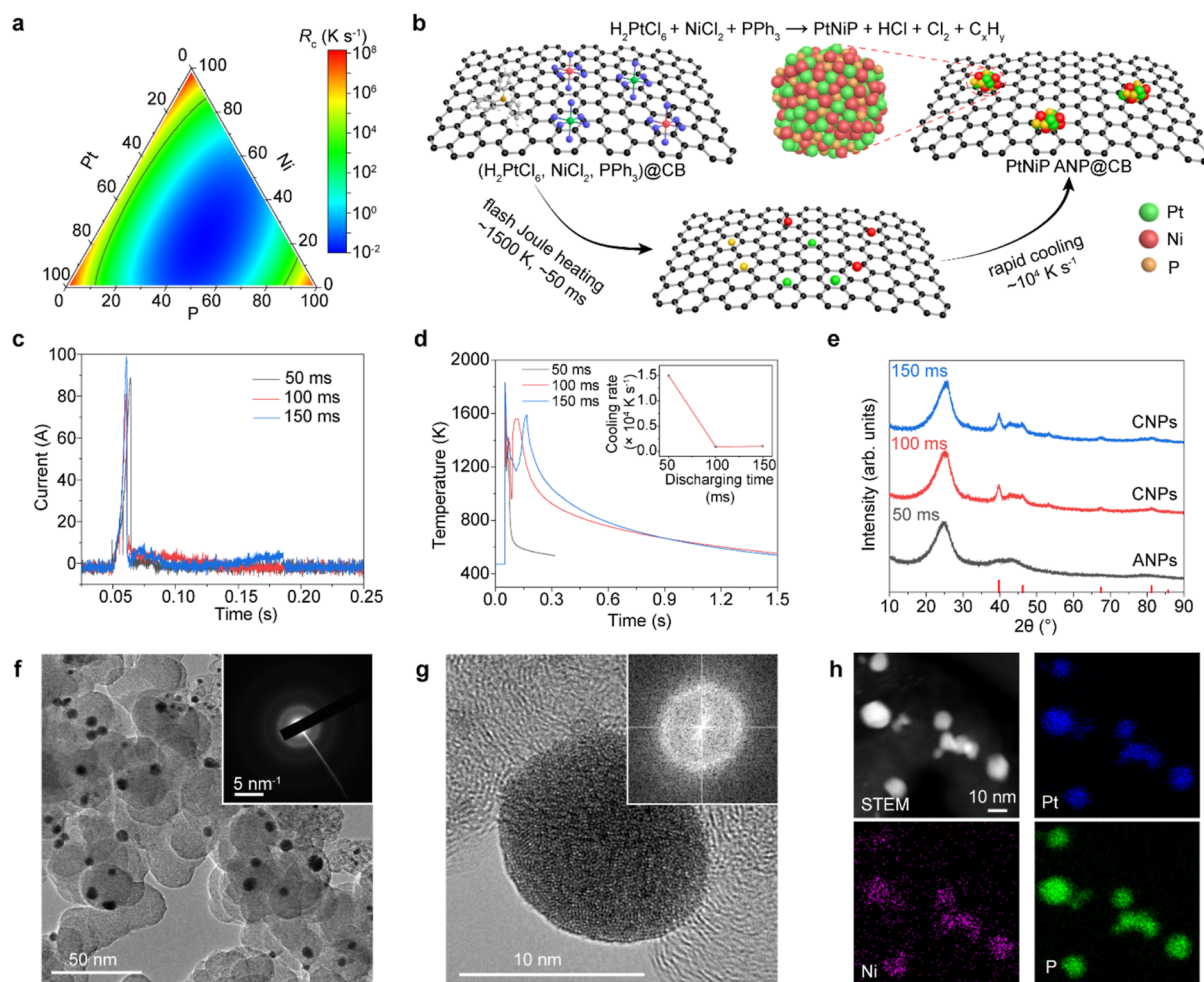
$$Q_{Cu}, Cu_{UPD} \rightarrow Cu^{2+} + 2e^- \tag{2}$$
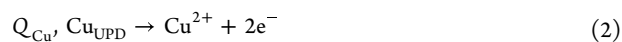
Figure 1. Synthesis of PtNiP ANPs by flash Joule heating. (a) Calculated R_C of the ternary Pt−Ni−P system. The dashed line denotes the $R_C = 10^4$ K s^{-1}. (b) Schematic of the FJH process for PtNiP ANP synthesis. (c) Pulsed current curve under the FJH conditions of 100 V at 50, 100, and 150 ms. (d) Real-time temperature curve recording using an infrared thermometer. Inset: cooling rate at different discharging times. (e) XRD patterns of PtNiP synthesized under different FJH durations. The Pt reference is shown (PDF#65-2868). (f) BF-TEM image of the PtNiP ANPs supported on carbon black. Inset, SAED pattern of the ANPs supported on carbon black. (g) HRTEM image of the PtNiP ANPs and corresponding fast Fourier transformation (FFT) image (inset). (h) HAADF-STEM images and EDS maps of the PtNiP ANPs.

$$n = Q_{Cu}/2F \tag{3}$$

where F is the Faraday constant (=96,485 C mol^{-1}).

Experimentally, the PtNiP ANPs catalyst was first polarized at 0.22, 0.23, 0.24, 0.25, 0.26, 0.27, 0.28, 0.29, and 0.30 V, respectively. Under the polarization potentials of 0.30−0.24 V, there is only a broad peak ranging from 0.3 to 0.6 V, which is attributed to the underpotentially deposited mono- or submonolayer Cu. When the potential decreases to 0.23 and 0.22 V, an oxidation peak appears at ~0.27 V, which is attributed to the oxidation of bulk Cu. Thus, 0.26 V was chosen as the potential for Cu UPD. The polarization curve at 0.26 V was also recorded in the absence of CuSO$_4$ (II). The Q_{Cu} was calculated by integrating the area between curves II and III. The active sites of other catalysts were measured similarly. The active sites of PtNi CNPs and commercial Pt/C were measured in the same way.

Turnover Frequency Calculation. The TOF per active site (s^{-1}) is calculated based on the following equation

$$TOF = I/(2Fn) \tag{4}$$

where I is the current during linear sweep measurement (A), F is the Faraday constant (=96,485 C mol^{-1}), and n is the number of active sites (mol). The factor 1/2 is based on the fact that two electrons are required to generate one hydrogen molecule.

Proton Exchange Membrane Water Electrolyzer Measurement. We used a self-made cell as the PEM-WE device[43] for water

electrolysis and the Nafion 117 membrane as the proton exchange membrane. To prepare the PtNiP ANPs-based HER cathode, ~0.65 mg cm^{-2} PtNiP ANPs catalyst with 20 wt % binder (Nafion 117) was airbrushed onto a carbon paper electrode. Commercially available IrO$_2$ anode (dioxide materials) was used as received without further treatment in our PEM-WE device. During the PEM-WE tests, the IrO$_2$ anode circulated with 0.5 M H$_2$SO$_4$ aqueous solution at 4 mL min^{-1} for the I−V curve test and 1 mL min^{-1} for stability tests. We measured the I−V curve in galvanostatic mode at 50−1000 mA cm^{-2} under room temperature and ambient pressure conditions. The stability tests were conducted at 250 and 1000 mA cm^{-2}, respectively, under room temperature and ambient pressure conditions.

Ab Initio Molecular Dynamics Simulation of Atomic Structures of PtNiP ANPs. The DFT method[44] implemented in the Vienna ab initio simulation package[45] was used. A plane wave expansion up to 500 eV was employed in combination with an all-electron-like projector augmented wave potential.[46] Exchange correlation was treated within the generalized gradient approximation using the functional parametrized by Perdew and Wang.[47] Three compositions with different P contents were calculated, namely, Pt$_{187}$Ni$_{187}$P$_{46}$ (P = 11 at %), Pt$_{168}$Ni$_{168}$P$_{84}$ (P = 20 at %), and Pt$_{140}$Ni$_{140}$P$_{140}$ (P = 33 at %). Surface structures of PtNiP MG with different compositions are searched based on the slab model. The thickness of the slabs is ~18 Å, and the slabs are separated by a 15 Å vacuum layer. Since the supercells are large enough, only Γ point was

used for the Brillouin zone integration over a Monkhorst—Pack-type mesh.[48] For structure optimization, the atoms were considered fully relaxed when the maximum force on each atom was less than 0.01 eV Å^{-1}. The bare surfaces are annealed at 1200 K and then cooled to 300 K at a rate of 200 K ps^{-1}. The MD simulations were performed using a Nose—Hoover thermostat and number—volume—temperature (NVT) ensemble.

Local Bond Orientational Order Parameters. Local bond orientational order (BOO) parameters (Q_4 and Q_6) were calculated based on the atomic structure models of PtNiP ANPs obtained by MD simulation, using an approach described before.[14,49] Following the previous method,[14] we defined a normalized BOO parameter as $\sqrt{Q_4^2 + Q_6^2}/\sqrt{Q_{4,fcc}^2 + Q_{6,fcc}^2}$, where $Q_{4,fcc}$ and $Q_{6,fcc}$ are the Q_4 and Q_6 parameters for perfect face-centered cubic (fcc) structures, respectively. This normalized BOO parameter is theoretically between 0 and 1, and a larger value demonstrates a more ordered atomic structure. The normalized BOO parameter value of 0.5 is adopted as the cutoff to distinguish the ordered and disordered structures.

Voronoi Tessellation Analysis and the Coordination Number Calculations. The Voronoi analysis of the atomic model of PtNiP ANPs was conducted using OVITO. A Voronoi polyhedron was analyzed for each atom based on the PtNiP atomic structure obtained by MD simulation. Because of the different coordination of metal and metalloids in PtNiP, we separately considered the Ni/Pt-centered polyhedra and the P-centered polyhedra. Each polyhedron was assigned a Voronoi index, $<n_3, n_4, n_5, n_6,...>$, where n_i represents the number of i-edged faces of the polyhedron. After the Voronoi index was obtained, the coordination number (CN) of the center atom was calculated from $\sum_i n_i$. The CN of each atom can also be calculated using the coordination analysis module in OVITO, which gives the same results.

DFT Calculation of Hydrogen Adsorption Energy. For H adsorption, H atoms are initially placed on both surfaces of the slab at a surface density of ~6.5 Å^2 per H atom, which is close to one monolayer on the Pt(111) surface, that is, 6.7 Å^2 per H atom. Then, the most energetically favorable pattern of H adsorption is searched by combining MD simulation at 300 K and post-MD optimization. It is found that the energy can be well converged after 5 ps of constant temperature MD, followed by cooling at a rate of 200 K ps^{-1}. Zero-point energies (ZPE) of hydrogen atoms adsorbed on the surface are calculated by calculating the vibrational frequencies of each adsorbed H atom on the surface with the surface fixed.

The Gibbs free energy (f_G) per hydrogen atom on the surface is expressed as

$$f_G = E_{bind} + E_{zp} - (E_{H_2} + en_{H_2})/2 \quad (5)$$

where E_{bind} is the binding energy per H on the surface, E_{H_2} is the total energy of an isolated hydrogen molecule, en_{H_2} is the entropy part of the hydrogen molecule in the gas state, and E_{zp} is the ZPE per H adsorbed on the surface. The binding energy is calculated with

$$E_{bind} = (E_{surf}^H - E_{surf})/n \quad (6)$$

where E_{surf}^H is the total energy of the metal surface with adsorbed H atoms, E_{surf} is the total energy of the clean metal surface, and n is the number of adsorbed H atoms. The entropy per hydrogen molecule at standard conditions is taken as $en_{H_2} = 0.3$ eV.[7] For calibration, we also modeled the properties of H adsorption on the crystalline Pt(111) and PtNi(111) surfaces. The ZPE on the Pt(111) surface is consistent with the experimental value of 0.14 eV.[8]

LCA and TEA. The environmental impact is evaluated via a cradle-to-gate LCA. Three scenarios were considered: the FJH process for PtNiP ANP production, pyrolysis for Pt CNP production, and reduction for Pt CNP production. The functional unit of this study is defined as the production of 1 g of Pt in PtNiP ANPs, where the utilization of Pt in Pt CNPs is calculated according to the mass activity difference. The system boundary is defined as the input of materials and output of the catalyst products. Waste management was not considered in this study. The life-cycle inventory (LCI) for inputs is from the ecoinvent database. The LCI entries were converted into environmental impacts using the ReCiPe 2016 methodology.[50] Eighteen environmental impacts were considered in this work. TEA was conducted using the same three scenarios. We considered only the operating costs in this study.

◼ RESULTS AND DISCUSSION

Synthesis of PtNiP ANPs by Flash Joule Heating. We began by conducting theoretical calculations to evaluate the amorphization potential of the ternary Pt—Ni—P system. Amorphous structures are in kinetically trapped metastable states derived from their crystallized phases. In thermal processes for producing amorphous materials, the critical cooling rate (R_C) determines whether a material forms in a crystalline or amorphous phase. We used an empirical model[51,52] to calculate the R_C for ternary PtNiP (Figure 1a; computational details in Text S1). Our results showed that R_C is strongly dependent on the P content: PtNiP compositions with 20—70 at % of P exhibit an $R_C < 10$ K s^{-1}, whereas compositions with <10 at % or >90 at % of P reach $R_C \sim 10^4$ K s^{-1}. Since the cooling rate of FJH exceeds 10^4 K s^{-1},[38,39] we hypothesized that FJH could enable the synthesis of amorphous PtNiP over a broad range of P content.

We thus designed a three-step process for synthesizing PtNiP ANPs (Figure 1b). First, precursors, including H$_2$PtCl$_6$, NiCl$_2$, and PPh$_3$, were dissolved in ethanol and loaded onto a carbon black support via wet impregnation (Figures 1b, left, and S1). The carbon black, with its appropriate resistance, served as both a conductive additive and a substrate (Figure S2). In the second step, during the FJH process, a pulsed current input was applied to rapidly raise the temperature of the sample, leading to the decomposition and fusion of the metal precursors (Figure 1b, middle), while the gaseous byproducts are released. Finally, the molten metal alloy melt vitrified into ANPs during the rapid cooling phase, driven by intensive thermal radiation[38,53] (Figure 1b, right).

Experimentally, the metal precursors mixed with carbon black were loaded into a quartz tube, and a pulse current was applied via an electrical system (Figure S3). We studied the effect of the pulsed current discharging time on the formation of amorphous structures. With a fixed voltage input of 100 V, we tested discharge times of 50, 100, and 150 ms (Figure 1c). The corresponding real-time temperature profiles were recorded (Figure 1d). While the maximum temperature remained similar across all conditions (Figure 1d), the cooling rate was strongly correlated with discharging time: at 50 ms, the cooling rate reached 1.5×10^4 K s^{-1}, but dropped to 100 K s^{-1} for both 100 and 150 ms durations (Figure 1d, inset). We further examined the impact of the discharging time on amorphization using the same Pt—Ni—P precursors. XRD patterns revealed that PtNiP synthesized at 50 ms displayed no crystalline peaks, whereas increasing the time to ≥100 ms led to the emergence of crystalline peaks by XRD (Figure 1e). Chloride precursor peaks were absent after the FJH reaction, indicating the complete conversion (Figure S4). No carbide phase is observed during the FJH synthesis.

This phenomenon of cooling-rate-dependent amorphization aligns well with our calculations (Figure 1a). According to the temperature-time-transformation diagram (Figure S5), the cooling rate dictates the formation of the amorphous phase. The cooling profiles for 100 and 150 ms durations intersected with the crystalline nose on the TTT diagram, resulting in the formation of crystalline phases. As a control, using the same
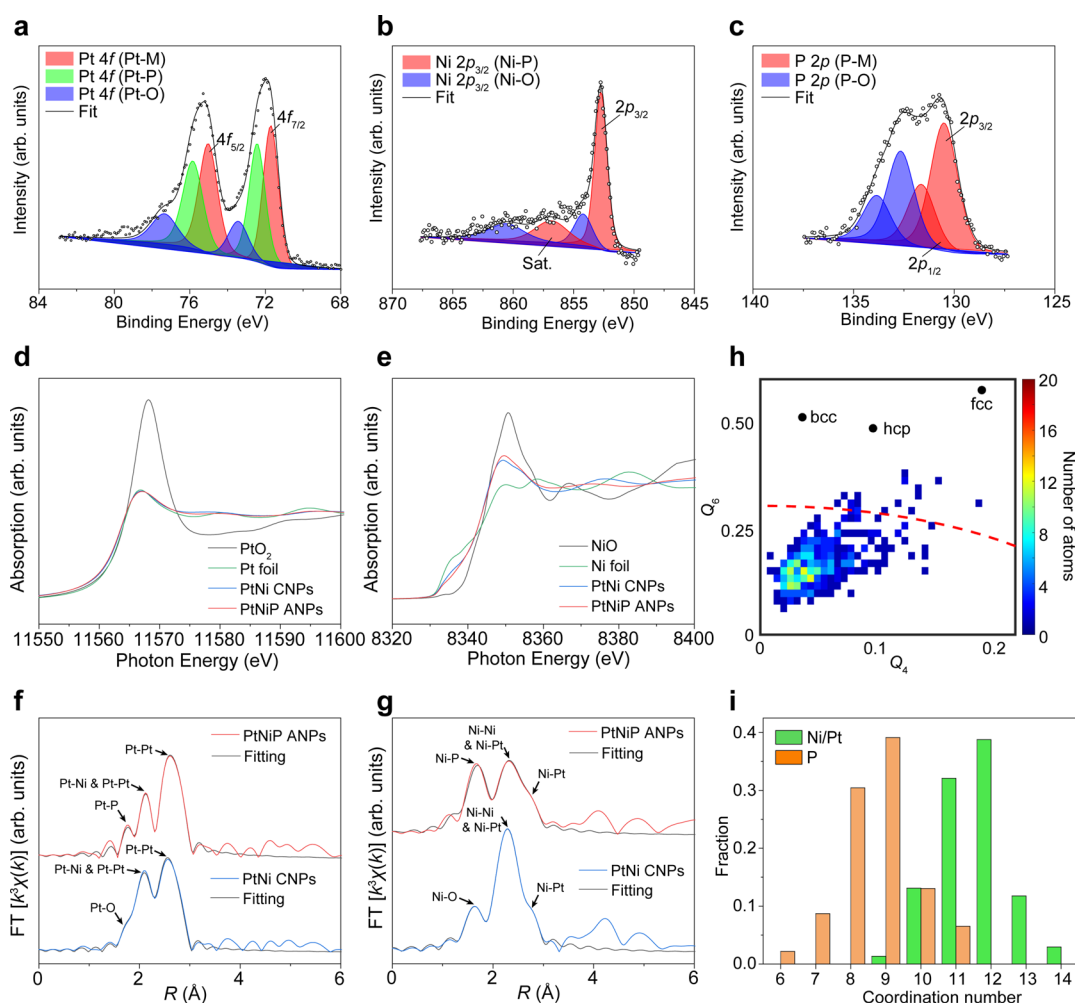
Figure 2. Characterization of the PtNiP ANPs. (a) XPS fine spectrum of Pt. (b) XPS fine spectrum of Ni. (c) XPS fine spectrum of P. (d) Normalized XANES spectra of PtO_2, Pt foil, PtNi CNPs, and PtNiP ANPs. (e) Normalized XANES spectra of NiO, Ni foil, PtNi CNPs, and PtNiP ANPs. (f) Pt L_3 edge FT-EXAFS spectra and fitting results of PtNi CNPs and PtNiP ANPs. (g) Ni K edge FT-EXAFS spectra and fitting results of PtNi CNPs and PtNiP ANPs. (h) Local BOO parameters of all the atoms in the amorphous PtNiP. The dashed red curves denote the normalized BOO parameter at 0.5, which serves as the criterion differentiating disordered and ordered structures. (i) CN distribution of Ni/Pt and P in the amorphous PtNiP. The average CN of Ni/Pt and P are 11.5 and 8.7, respectively.

Pt–Ni–P precursors in a conventional tube furnace with a slow cooling rate of ~10 K min^{-1} only produced crystalline nanoparticles (CNPs; Figure S6). Besides cooling rate, we found that P content strongly influences the formation of amorphous structure.[54] As a control, under the same FJH conditions, Pt precursor or Pt–Ni precursors resulted in Pt CNPs or PtNi CNPs, respectively (Figures S7 and S8), highlighting the crucial role of P in ANP formation. These results clearly demonstrate that the synthesis of PtNiP ANPs is kinetically controlled by ultrafast cooling. We note that the high temperature of FJH can increase the crystallinity of a material, such as graphene,[55] but in our case, the synthesis of PtNiP ANPs is dominated by the ultrafast cooling of FJH.

Characterization of the PtNiP ANPs. The morphology and amorphous structure of the PtNiP ANPs were carefully studied by using several characterization techniques. Transmission electron microscopy (TEM) was used to confirm the amorphous nature of the PtNiP nanoparticles (Figure 1f,g). The as-synthesized nanoparticles were well dispersed on the carbon black substrates (Figures 1f and S9). SAED revealed diffusive halos with no discrete spots (Figure 1f, inset), a characteristic feature of amorphous materials. The amorphous

structure was further corroborated by HRTEM, where no lattice fringes were observed (Figure 1g). The corresponding FFT pattern showed diffraction halos (Figure 1g, inset), consistent with the SAED results. The PtNiP ANPs had an average size of ~10.5 nm with a narrow size distribution (Figure S10), demonstrating the precise size control enabled by the FJH process. The elemental composition was determined by energy-dispersive X-ray spectroscopy (EDS; Figure S11). It shows the existence of Pt, Ni, and P and the absence of Cl. HAADF-STEM images and corresponding element maps showed uniform distributions of Pt, Ni, and P throughout the nanoparticles (Figure 1h). In contrast, nanoparticles synthesized using a 100 ms FJH duration showed a mixture of partially and fully crystallized particles (Figure S12), while further extending the time to 150 ms led to the formation of fully crystalline PtNiP CNPs (Figure S13).

We then investigated the electronic structures of PtNiP ANPs using XPS. Various chemical bonds were identified, including Pt–Pt, Ni–Ni, P–P, Pt–Ni, Pt–P, and Ni–P, which are attributed to the amorphous structure (Figure 2a–c and Table S1). The Pt 4f spectrum was split into the $4f_{7/2}$ and $4f_{5/2}$ components. The $Pt_{7/2}$ peak at 71.6 eV corresponds to Pt
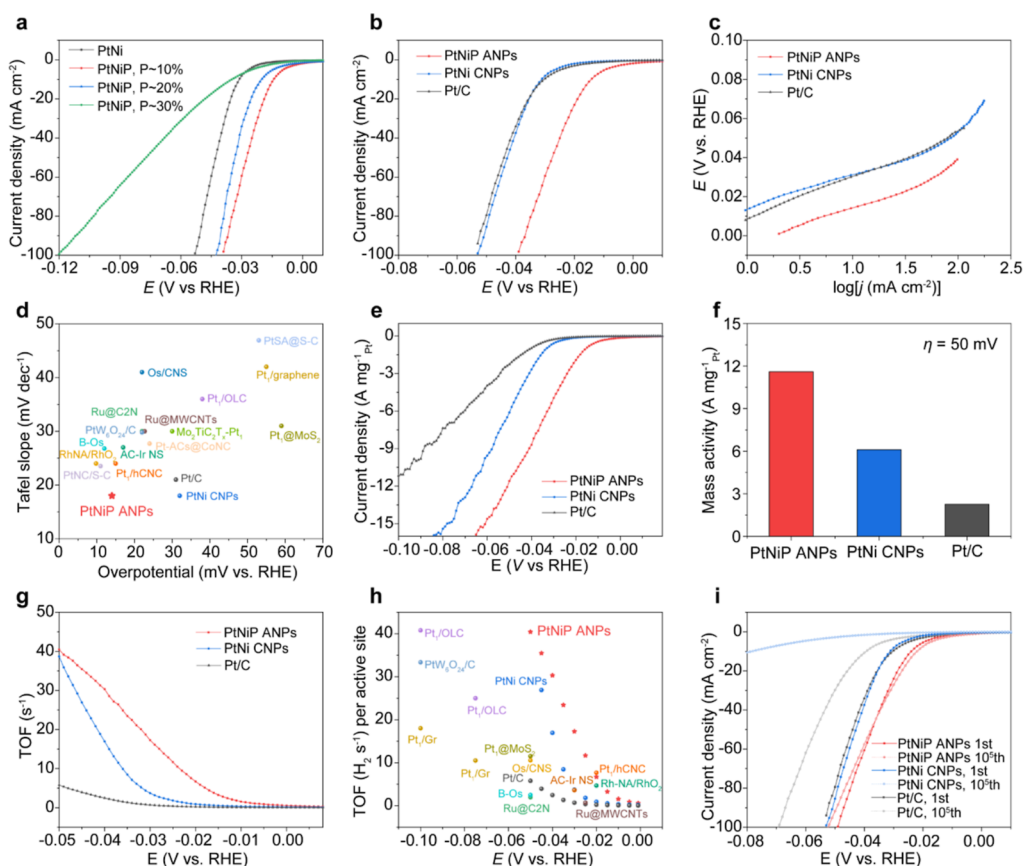
Figure 3. Performance of PtNiP ANPs in electrocatalytic hydrogen evolution. (a) Polarization curves of PtNi CNPs and PtNiP ANPs with different P molar ratios. (b) Polarization curves of PtNiP ANPs with $P \sim 10$ at %, PtNi CNPs, and commercial Pt/C. (c) Tafel plots derived from the polarization curves. (d) Performance (overpotential at 10 mV dec^{-1} and Tafel slope) comparison between this work and recent reported precious metal-based catalysts for HER. The data and references are shown in Table S4. All the measurements were conducted in 0.5 M H$_2$SO$_4$ by dropping the electrocatalysts on a glassy carbon electrode using a three-electrode configuration. (e) Polarization curves of PtNiP ANPs, PtNi CNPs, and commercial Pt/C normalized to the mass loading of Pt. (f) Mass activity of PtNiP ANPs, PtNi CNPs, and commercial Pt/C normalized to the Pt loading at overpotential of 30 mV with respect to RHE. (h) Comparison of TOF with literature. The data and references are shown in Table S4. (i) Polarization curves for PtNiP ANPs, PtNi CNPs, and commercial Pt/C at the first cycle and after 10,000th CV cycling.

metal (including Pt–Pt and Pt–Ni[56]), the 72.6 eV peak is assigned to Pt–P,[57] and the 73.7 eV peak is attributed to Pt–O[58] resulting from surface oxidation (Figure 2a). The peak at 852.7 eV is assigned to Ni 2p$_{3/2}$ in Ni–P, while the peak at 856.8 eV represents a satellite peak[59] (Figure 2b). The peak at 854.2 eV is assigned to Ni 2p$_{3/2}$ in Ni–O, again due to surface oxidation. For P 2p$_{3/2}$, the peak at 130.5 eV is assigned to P-metal (including P–Pt and P–Ni[60]), while the peak at 132.7 eV corresponds to P–O[61] (Figure 2c).

Next, we employed X-ray absorption spectroscopy (XAS) to investigate the coordination environment of PtNiP ANPs, with PtNi CNPs being used as a comparison. The normalized XANES results for the Pt L-edge (Figure 2d) show the white-line intensities of PtNi CNPs and PtNiP ANPs are similar to that of Pt foil and lower than that of PtO$_2$, indicating that the Pt species in both PtNi and PtNiP are close to their metal state. The normalized XANES results of the Ni K-edge (Figure 2e) show that the absorption edges of PtNi CNPs and PtNiP ANPs are positioned between those of Ni foil and NiO, indicating that the valence states of Ni species in both PtNi and PtNiP are lower than +2. The oxidation of Pt and Ni in PtNi CNPs is likely caused by the surface oxidation of the nanoparticles. EXAFS analysis of the Pt L_3 edge revealed the presence of Pt–Pt, Pt–Ni, and Pt–P bonds in PtNiP ANPs

(Figure 2f, with fitting results in Table S2), while the Ni K-edge spectra confirmed the presence of Ni–Pt, Ni–Ni, and Ni–P bonds (Figure 2g, and with fitting results in Table S3). These results demonstrate the existence of various coordination environments for Pt and Ni species, a hallmark of disordered structures. Moreover, we found that P preferentially coordinates with Ni rather than Pt (Figure 2f,g), which fine-tuned the electronic structure of Pt.

To further investigate the detailed local coordination information on PtNiP ANPs, ab initio MD simulation was implemented to explore their atomic structure. Three compositions with varying P content (11, 20, and 33 atom %) were modeled (Figure S14), with the composition at 11 atom % of P being extensively analyzed (Figure S14a). The local BOO was employed to quantitatively describe the degree of structural disorder.[14,49] Results showed that 96.2% of atoms in the PtNiP ANPs were disordered under the criterion of normalized BOO parameters (Figure 2h). Voronoi tessellation was further conducted to evaluate the coordination of each atom in the PtNiP ANPs.[14,54,62] Since metals like Ni and Pt and metalloids like P typically exhibit distinct local orders,[54] they were considered separately. The ten most abundant Ni/Pt-centered Voronoi polyhedra in amorphous PtNiP are depicted (Figure S15). From the Voronoi analysis, the
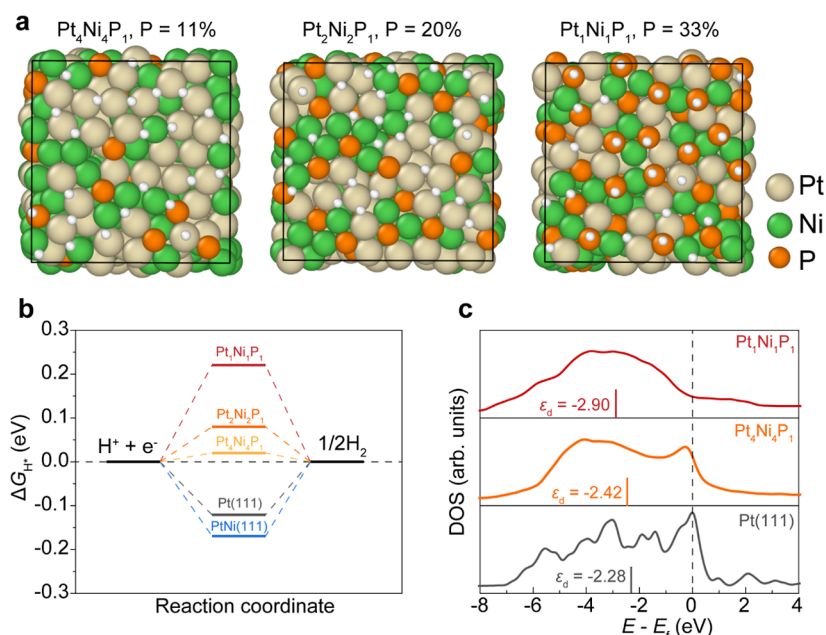
Figure 4. Mechanism of the HER performance. (a) MD simulated structures and hydrogen adsorption configurations for amorphous PtNiP with compositions of $Pt_4Ni_4P_1$, $Pt_2Ni_2P_1$, and $Pt_1Ni_1P_1$. (b) Calculated free−energy diagram of hydrogen adsorption at the equilibrium potential for crystalline Pt(111), crystalline PtNi(111), and amorphous PtNiP with different compositions. (c) Density of states (DOS) of d orbitals of the active Pt on crystalline Pt(111), crystalline PtNi(111), and amorphous PtNiP. The d band center positions relative to the E_f were labeled.

coordination numbers of all atoms in the amorphous PtNiP were determined based on the Voronoi index from $\sum_i n_i$ (Figure 2i). The average CN of Ni/Pt is 11.5, which is lower than the 12 seen in the close-packed crystalline structures. The lower CN is a typical feature of amorphous materials, further confirming the amorphous structure of PtNiP.

The carbon substrates are important for the self-heating and ultrafast cooling, so our current synthesis is limited to carbon substrates and not compatible with nonconductive inorganic substrates, like SiO_2 and Al_2O_3.

Application of PtNiP ANPs as High-Performance HER Catalysts. Leveraging an easily tunable precursor loading and ultrafast synthesis, FJH provides access to a vast compositional space of PtNiP ANPs. To demonstrate their practical applicability, we here explored PtNiP ANPs as high-perform-ance electrocatalysts for the HER. HER activity was evaluated in a standard three-electrode setup in a N_2-saturated 0.5 M H_2SO_4 using an RDE. A series of PtNiP ANPs with P contents ranging from 10% to 30% were synthesized, with PtNi CNPs used as a comparison.

We found that the catalytic performance of PtNiP ANPs strongly correlated with the P content (Figure 3a). Three compositions with P contents at ∼10%, ∼20%, and ∼30% were synthesized, with optimal performance at ∼10%, indicating an increased electrocatalytic performance along with the decrease of P content. We were unable to further explore the P content <10% since current FJH synthesis cannot enable the production of PtNiP ANPs at P < 10% (Figure 1a). To further assess the performance, high-quality commercial Pt/C was used as a reference. Polarization curves (Figure 3b) indicated that the PtNiP ANPs exhibit a very low overpotential (η) of ∼14 mV to deliver 10 mA cm^{-2}, lower than PtNi CNPs (∼22 mV) and commercial Pt/C (∼21 mV). Additionally, PtNiP ANPs achieved a Tafel slope of only 18 mV dec^{-1} (Figure 3c), outperforming Pt/C (21 mV dec^{-1}) and

suggesting the dominant Volmer−Tafel mechanism, with recombination of chemisorbed H* as the rate-determining step.[7] Based on the overpotential and Tafel slope, PtNiP ANPs are among the best precious-metal-based catalysts reported (Figure 3d and Table S4). We further normalized the polarization curves based on the Pt mass loading (Figure 3e), which was calculated by ICP−MS (see details in the Section Methods). At η = 50 mV, PtNiP ANPs deliver a mass activity of 11.6 A mg$^{-1}_{Pt}$, which is ∼1.9 and ∼5.1 times higher than PtNi NPs and Pt/C, respectively (Figure 3f and Table S5). This indicates that the Pt loading can be substantially reduced using our amorphization and compositional opti-mization strategy.

We then investigated factors dominating the origin of this superior HER performance of PtNiP ANPs. First, the ECSA was measured (Figure S16 and Table S6). Despite the better HER performance of PtNiP ANPs, their ECSA was smaller than that of Pt/C, indicating that active surface area was not the primary factor behind their superior catalytic performance. Second, we calculated the active sites (Figure S17, see details in Section Methods), based on which the turnover frequency (TOF) per active site was measured to evaluate intrinsic catalytic ability (Figure 3g, see details in Section Methods). The TOF values for PtNiP ANPs at 20 and 50 mV (vs RHE) were 6.71 and 40.5 H$_2$ s^{-1}, respectively, significantly higher than those for Pt/C (0.22 H$_2$ s^{-1} at 20 mV; 5.84 H$_2$ s^{-1} at 50 mV), placing PtNiP ANPs among the top Pt-group metal nanocatalysts (Figure 3h and Table S4). Third, electrode kinetics for proton reduction were investigated using electro-chemical impedance spectroscopy under η = 20 mV. The Nyquist plots showed that PtNiP ANPs exhibit a charge transfer resistance of ∼13 Ω, lower than that of Pt/C at 21 Ω (Figure S18), demonstrating a fast Faradaic process at the catalyst−electrolyte interface. Together, these findings dem-onstrate that the superior HER performance of PtNiP ANPs stems from their intrinsically high activity.
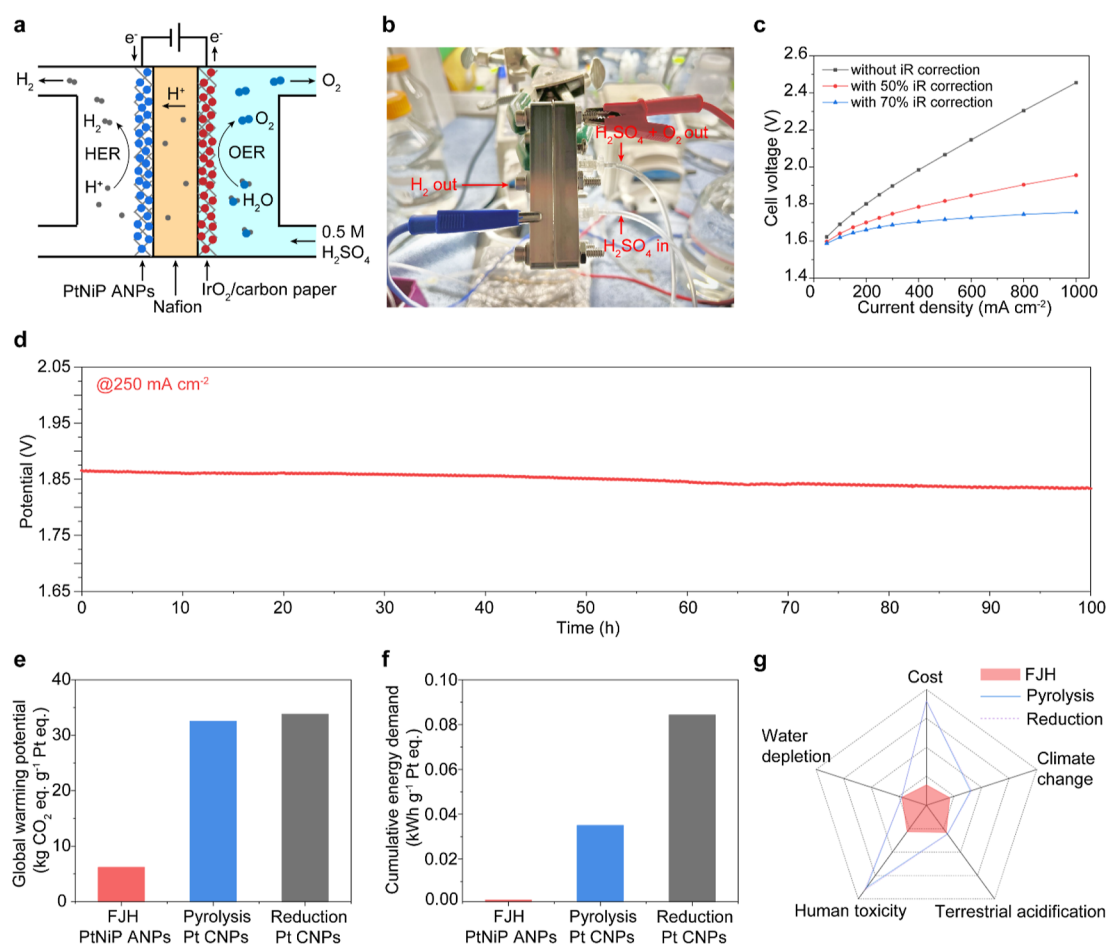
Figure 5. Practical application, sustainability, and TEA. (a) Schematic showing the configuration of the PEM electrolyzer. (b) Photograph of the 1 cm^2 PEM electrolyzer test station. (c) Polarization curves of the PEM electrolyzer. (d) Durability voltage−time plots for the PEM electrolyzer. (e,f) Global warming potential (GWP) (e) and cumulative energy demand (CED) (f) of three scenarios: FJH PtNiP ANPs, Pyrolysis Pt CNPs, and Reduction Pt CNPs. (g) Radar plot comparing the three processes regarding climate change, terrestrial acidification, human toxicity, water depletion, and cost. The functional unit for the LCA and TEA analysis is 1 g Pt equivalent in PtNiP ANPs.

Durability is crucial for practical applications. The stability of the PtNiP ANP catalysts was tested by using RDE. The accelerated CV aging test demonstrated negligible performance loss of PtNiP ANPs (Figure 3i). After 10,000 CV cycles, the overpotential at 10 mA cm^{-2} slightly decreased from 24 to 22 mV. In contrast, the overpotential for Pt/C increased from 30 to 40 mV, and for PtNi CNPs, from 31 to 79 mV. These observations demonstrated the superior stability of the PtNiP ANPs. A chronopotentiometry test was also conducted, which further confirmed the excellent stability of the PtNiP ANPs for the HER (Figure S19). Postcatalysis characterizations by TEM (Figure S20) and XPS (Figure S21) indicated that the structure, size, and properties of PtNiP ANPs were well maintained, demonstrating the long-term viability and robustness of the PtNiP ANP catalyst.

Mechanism of the HER Performance. To gain atomic-level insight into the origin of the high intrinsic activity of PtNiP ANPs for HER, DFT calculations were performed. To elucidate the critical role of the amorphous structure and P content, we constructed atomic models of three PtNiP compositions: $Pt_4Ni_4P_1$ (~11% P), $Pt_2Ni_2P_1$ (~20% P), and $Pt_1Ni_1P_1$ (~33% P), based on molecular dynamic simulations (Figure S14). MD was performed to construct the amorphous atomic structures by rapid cooling (see details in the Section Methods). These amorphous structures are isotropic on all

surfaces. Crystalline Pt(111) and PtNi(111) surfaces were used for comparison (Figure S22).

For the acidic HER process, the hydrogen adsorption Gibbs free energy (ΔG_{H*}) is commonly adopted as the descriptor for evaluating the intrinsic catalytic activity. The most energetically favorable hydrogen adsorption pattern was identified through MD simulations at 300 K, followed by post-MD optimization (Figures 4a and S23). According to the Sabatier principle, active sites with |ΔG_{H*}| values close to zero optimize the balance between hydrogen adsorption and desorption, enhancing catalytic efficiency.[63] The energy diagram of various catalysts (Figure 4b and Table S7) shows that alloying Ni with Pt increases the hydrogen interaction, leading to a negative shift in ΔG_{H*} for PtNi(111) compared to Pt(111). In contrast, the addition of P weakens hydrogen binding as P content increases. Notably, the ΔG_{H*} values of $Pt_2Ni_2P_1$ (0.08 eV) and $Pt_4Ni_4P_1$ (0.02 eV) are close to the ideal thermoneutral state, even better than the Pt(111) surface (−0.12 eV). These results align with the experimentally optimized P content (Figure 3a), highlighting the excellent intrinsic catalytic performance of the PtNiP ANPs.

To further elucidate the superior activity of PtNiP ANPs, the electronic structures were examined. We calculated the DOS of $Pt_1Ni_1P_1$, $Pt_4Ni_4P_1$, and Pt(111) (Figure 4c). The d orbitals of PtNiP ANPs were shifted to the left relative to that of Pt(111)

(Figure 4c). The introduction of P lowers the d-band center (ε_d) of Pt atoms in amorphous PtNiP below the Fermi level. The ε_d of $Pt_4Ni_4P_1$ is lower than that of Pt(111) by -0.14 eV, resulting in a weaker binding to H*, according to the d-band theory.[64] These theoretical calculations confirm the critical roles of amorphization and compositional optimization in enhancing the catalytic performance of PtNiP ANPs.

The energy diagram (Figure 4b) implies that an ideal HER performance can be potentially achieved by further optimizing the P content in the ternary PtNiP ANPs. While we are unable to synthesize PtNiP ANPs with $P < 10\%$ due to the cooling rate limit of FJH (Figure 1a), we here deployed theoretical calculation to explore this. Briefly, we modeled the atomic structures of $Pt_9Ni_9P_1$ ($P \sim 5.2\%$) and $Pt_{20.5}Ni_{20.5}P_1$ ($P \sim 2.4\%$) (Figure S24), and their ΔG_{H*} values were also calculated (Figure S25a and Table S7). The ΔG_{H*} versus P molar ratio plot shows a typical volcano feature (Figure S25b). ΔG_{H*} may approach absolute zero at a P content of $\sim$7%.

Practical Application and Environmental and Technoeconomic Considerations. To show the practical application potential of PtNiP ANPs for green hydrogen production, we assembled a proton exchange membrane water electrolyzer (PEM-WE) using PtNiP ANPs as a cathode catalyst for HER, commercial IrO_2 as an anode catalyst for the oxygen evolution reaction (OER), and a Nafion 117 membrane for proton transfer (Figure 5a,b). IrO_2 was chosen due to its well-known high OER stability for practical PEM-WE applications.[65] The current–voltage ($I–V$) curve shows that the PtNiP ANPs-based PEM-WE required 1.85, 2.06, and 2.45 V to drive water electrolysis current densities of 250, 500, and 1000 mA cm^{-2}, respectively, without iR compensation (Figure 5c). We note that due to the limitations in our setup for fabricating an industrial-quality membrane electrode between the cathode and anode to minimize ionic resistance, our assembled electrolyzer exhibited a relatively high impedance of $\sim$0.7 Ω cm^{-2}. Performance could be improved by reducing the cell resistance. For example, with 70% iR correction, the PEM-WE device delivered 1 A cm^{-2} at only 1.75 V, comparable to state-of-the-art water electrolyzers.[66] The stability of the catalyst is crucial for practical applications. Notably, the PtNiP ANP-based PEM-WE can operate stably for 100 h at 250 mA cm^{-2} without any significant increase in the cell voltage (Figures 5d and S26).

To examine the environmental impact of the FJH process for producing amorphous catalysts, a preliminary LCA was conducted (details in the Section Methods). Two traditional thermal processes for Pt CNPs catalyst production, namely, pyrolysis and reduction, were used as comparison (Figure S27 and Table S8), using the production of 1 g of Pt equivalent (eq) in PtNiP ANPs as the functional unit. Both material use and energy consumption were considered. The environmental impact of the FJH process was significantly lower than that of the traditional processes (Figures S28−S30 and Tables S9−S12). Specifically, the GWP of FJH-produced PtNiP ANPs was estimated at 6.2 kg of CO_2 eq per g of Pt eq, representing an $\sim$80% reduction compared to traditional methods (Figure 5e and Tables S9−S12). Due to the high energy efficiency of the FJH process (Text S2), the CED of our process was calculated to be only 0.0017 kWh per g of Pt eq, which is just 2−5% of the energy required for the pyrolysis and reduction processes (Figure 5f).

Lastly, in evaluating the economic feasibility, a TEA was conducted to compare the operating costs of producing PtNiP

ANP catalysts with these conventional processes for commercial Pt/C catalysts (Figure S27 and Table S13). The production of PtNiP ANPs was estimated to be $\sim$\$32 per g of Pt equiv, representing an $\sim$80% reduction compared to Pt/C produced by conventional processes (Figure S27). Given the high intrinsic catalytic activity of PtNiP ANPs, the energy efficiency of the FJH process, and its water-free feature, this approach demonstrates significant potential for both sustainability and economic viability compared with existing commercial methods (Figure 5g).

CONCLUSIONS

In summary, we developed a new method for synthesizing PtNiP ANPs with widely tunable compositions using the FJH process, featuring ultrafast heating and cooling rates. The resulting PtNiP ANPs exhibit an exceptional intrinsic catalytic performance for hydrogen production. We anticipate that this process could be extended to the synthesis of a broad range of amorphous materials, pushing the boundaries of the currently crystalline phase-dominated materials discovery. Additionally, the combination of amorphization and composition optimization presents a new paradigm for catalyst design, contributing to the search for high-performance materials in other catalysis reactions.

ASSOCIATED CONTENT

Ⓢ Supporting Information

The Supporting Information is available free of charge at https://pubs.acs.org/doi/10.1021/jacs.5c00071.

> Additional discussion on calculation of the critical cooling rate, calculation of energy consumption, LCA, and techno-economic analysis (PDF)

AUTHOR INFORMATION

Corresponding Authors

Bing Deng − *School of Environment and State Key Laboratory of Iron and Steel Industry Environment Protection, Tsinghua University, Beijing 10084, China; Department of Chemistry, Rice University, Houston, Texas 77005, United States;* ⓞ orcid.org/0000-0003-0530-8410; Email: dengbing@tsinghua.edu.cn

Haotian Wang − *Department of Chemistry, Rice University, Houston, Texas 77005, United States; Department of Chemical and Biomolecular Engineering and Department of Materials Science and NanoEngineering, Rice University, Houston, Texas 77005, United States;* ⓞ orcid.org/0000-0002-3552-8978; Email: htwang@rice.edu

Yufeng Zhao − *Corban University, Salem, Oregon 97317, United States; Department of Materials Science and NanoEngineering and Smalley-Curl Institute, Rice University, Houston, Texas 77005, United States;* Email: YZhao@corban.edu

James M. Tour − *Department of Chemistry, Rice University, Houston, Texas 77005, United States; Department of Materials Science and NanoEngineering, Smalley-Curl Institute, and NanoCarbon Center and the Rice Advanced Materials Institute, Rice University, Houston, Texas 77005, United States;* ⓞ orcid.org/0000-0002-8479-9328; Email: tour@rice.edu

Authors

Zhen-Yu Wu − *Department of Chemical and Biomolecular Engineering, Rice University, Houston, Texas 77005, United States; Present Address: Department of Chemistry, Institute of Innovative Material, Guangdong Provincial Key Laboratory of Sustainable Biomimetic Materials and Green Energy, Southern University of Science and Technology, Shenzhen 518055, Guangdong, PR China;* orcid.org/0000-0001-9198-003X

Erkang Feng − *School of Environment, Tsinghua University, Beijing 10084, China*

Lu Ma − *National Synchrotron Light Source II (NSLS-II), Brookhaven National Laboratory, Upton, New York 11973, United States*

Zhe Wang − *Department of Chemistry, Rice University, Houston, Texas 77005, United States; Present Address: Department of Chemical and Biochemical Engineering, The University of Iowa, Iowa City, Iowa 52242, United States.*

Jinhang Chen − *Department of Chemistry, Rice University, Houston, Texas 77005, United States*

Lucas Eddy − *Department of Chemistry, Rice University, Houston, Texas 77005, United States; Applied Physics Program and Smalley-Curl Institute, Rice University, Houston, Texas 77005, United States*

Alexander Lathem − *Department of Chemistry, Rice University, Houston, Texas 77005, United States; Applied Physics Program and Smalley-Curl Institute, Rice University, Houston, Texas 77005, United States*

Teng Wang − *School of Environment, Tsinghua University, Beijing 10084, China; Tanwei College, Tsinghua University, Beijing 10084, China;* orcid.org/0009-0001-6129-0449

Weiyin Chen − *Department of Chemistry, Rice University, Houston, Texas 77005, United States; Present Address: Department of Nuclear Science and Engineering, Massachusetts Institute of Technology, 77 Massachusetts Avenue, Cambridge, MA 02139, United States.;* orcid.org/0000-0002-6427-4129

Yi Cheng − *Department of Chemistry, Rice University, Houston, Texas 77005, United States*

Shichen Xu − *Department of Chemistry, Rice University, Houston, Texas 77005, United States*

Qiming Liu − *Department of Chemistry, Rice University, Houston, Texas 77005, United States;* orcid.org/0000-0001-5839-5453

Boris I. Yakobson − *Department of Chemistry, Rice University, Houston, Texas 77005, United States; Department of Materials Science and NanoEngineering and Smalley-Curl Institute, Rice University, Houston, Texas 77005, United States;* orcid.org/0000-0001-8369-3567

Complete contact information is available at:
https://pubs.acs.org/10.1021/jacs.5c00071

Author Contributions

§§B.D. and Z.-Y.W. contributed equally.

Notes

The authors declare no competing financial interest.

■ REFERENCES

(1) Zhu, J.; Hu, L.; Zhao, P.; Lee, L. Y. S.; Wong, K.-Y. Recent advances in electrocatalytic hydrogen evolution using nanoparticles. *Chem. Rev.* **2020**, *120* (2), 851−918.

(2) Maestre, V. M.; Ortiz, A.; Ortiz, I. Challenges and prospects of renewable hydrogen-based strategies for full decarbonization of stationary power applications. *Renewable Sustainable Energy Rev.* **2021**, *152*, 111628.

(3) Li, F.; Guo, Z.; Song, Z.; Wang, L.; Zheng, L.; Cheng, G.; Mattevi, C.; Hong, Z.; Titirici, M.-M. Ultrafast synthesis of battery grade graphite enabled by a multi-physics field carbonization. *Chem. Eng. J.* **2023**, *461*, 142128.

(4) Mahmood, J.; Li, F.; Jung, S.-M.; Okyay, M. S.; Ahmad, I.; Kim, S.-J.; Park, N.; Jeong, H. Y.; Baek, J.-B. An efficient and pH-universal ruthenium-based catalyst for the hydrogen evolution reaction. *Nat. Nanotechnol.* **2017**, *12* (5), 441−446.

(5) Wang, J.-H.; Yang, S.-W.; Ma, F.-B.; Zhao, Y.-K.; Zhao, S.-N.; Xiong, Z.-Y.; Cai, D.; Shen, H.-D.; Zhu, K.; Zhang, Q.-Y.; Cao, Y.-L.; Wang, T.-S.; Zhang, H.-P. RuCo alloy nanoparticles embedded within N-doped porous two-dimensional carbon nanosheets: a high-performance hydrogen evolution reaction catalyst. *Tungsten* **2024**, *6* (1), 114−123.

(6) Zhang, J.; Zhao, Y.; Guo, X.; Chen, C.; Dong, C.-L.; Liu, R.-S.; Han, C.-P.; Li, Y.; Gogotsi, Y.; Wang, G. Single platinum atoms immobilized on an MXene as an efficient catalyst for the hydrogen evolution reaction. *Nat. Catal.* **2018**, *1* (12), 985−992.

(7) Liu, D.; Li, X.; Chen, S.; Yan, H.; Wang, C.; Wu, C.; Haleem, Y. A.; Duan, S.; Lu, J.; Ge, B.; Ajayan, P. M.; Luo, Y.; Jiang, J.; Song, L. Atomically dispersed platinum supported on curved carbon supports for efficient electrocatalytic hydrogen evolution. *Nat. Energy* **2019**, *4* (6), 512−518.

(8) Zhao, Z.; Liu, H.; Gao, W.; Xue, W.; Liu, Z.; Huang, J.; Pan, X.; Huang, Y. Surface-engineered PtNi-O nanostructure with record-high performance for electrocatalytic hydrogen evolution reaction. *J. Am. Chem. Soc.* **2018**, *140* (29), 9046−9050.

(9) Zhao, Z.; Liu, Z.; Zhang, A.; Yan, X.; Xue, W.; Peng, B.; Xin, H. L.; Pan, X.; Duan, X.; Huang, Y. Graphene-nanopocket-encaged PtCo nanocatalysts for highly durable fuel cell operation under demanding ultralow-Pt-loading conditions. *Nat. Nanotechnol.* **2022**, *17* (9), 968−975.

(10) Wu, G.; Han, X.; Cai, J.; Yin, P.; Cui, P.; Zheng, X.; Li, H.; Chen, C.; Wang, G.; Hong, X. In-plane strain engineering in ultrathin noble metal nanosheets boosts the intrinsic electrocatalytic hydrogen evolution activity. *Nat. Commun.* **2022**, *13* (1), 4200.

(11) Fan, Z.; Liao, F.; Ji, Y.; Liu, Y.; Huang, H.; Wang, D.; Yin, K.; Yang, H.; Ma, M.; Zhu, W.; Wang, M.; Kang, Z.; Li, Y.; Shao, M.; Hu,

Z.; Shao, Q. Coupling of nanocrystal hexagonal array and two-dimensional metastable substrate boosts H2-production. *Nat. Commun.* **2022**, *13* (1), 5828.

(12) Kang, J.; Yang, X.; Hu, Q.; Cai, Z.; Liu, L.-M.; Guo, L. Recent progress of amorphous nanomaterials. *Chem. Rev.* **2023**, *123* (13), 8859–8941.

(13) Yuan, Y.; Kim, D. S.; Zhou, J.; Chang, D. J.; Zhu, F.; Nagaoka, Y.; Yang, Y.; Pham, M.; Osher, S. J.; Chen, O.; Ercius, P.; Schmid, A. K.; Miao, J. Three-dimensional atomic packing in amorphous solids with liquid-like structure. *Nat. Mater.* **2022**, *21* (1), 95–102.

(14) Yang, Y.; Zhou, J.; Zhu, F.; Yuan, Y.; Chang, D. J.; Kim, D. S.; Pham, M.; Rana, A.; Tian, X.; Yao, Y.; Osher, S. J.; Schmid, A. K.; Hu, L.; Ercius, P.; Miao, J. Determining the three-dimensional atomic structure of an amorphous solid. *Nature* **2021**, *592* (7852), 60–64.

(15) Zhou, Y.; Hao, W.; Zhao, X.; Zhou, J.; Yu, H.; Lin, B.; Liu, Z.; Pennycook, S. J.; Li, S.; Fan, H. J. Electronegativity-induced charge balancing to boost stability and activity of amorphous electrocatalysts. *Adv. Mater.* **2022**, *34* (20), 2100537.

(16) Lou, Y.; Yao, Z.; Fu, S.; Liu, S.; Zhu, X.; Huang, W.; Dong, M.; Zeng, J.; Lin, H.; Zhu, H.; Lan, S. Pd–Ni–P metallic glass nanoparticles for nonenzymatic glucose sensing. *Prog. Nat. Sci.: Mater. Int.* **2023**, *33* (2), 244–249.

(17) Wu, G.; Zheng, X.; Cui, P.; Jiang, H.; Wang, X.; Qu, Y.; Chen, W.; Lin, Y.; Li, H.; Han, X.; Hu, Y.; Liu, P.; Zhang, Q.; Ge, J.; Yao, Y.; Sun, R.; Wu, Y.; Gu, L.; Hong, X.; Li, Y. A general synthesis approach for amorphous noble metal nanosheets. *Nat. Commun.* **2019**, *10* (1), 4855.

(18) Ge, Y.; Huang, Z.; Ling, C.; Chen, B.; Liu, G.; Zhou, M.; Liu, J.; Zhang, X.; Cheng, H.; Liu, G.; Du, Y.; Sun, C.-J.; Tan, C.; Huang, J.; Yin, P.; Fan, Z.; Chen, Y.; Yang, N.; Zhang, H. Phase-selective epitaxial growth of heterophase nanostructures on unconventional 2H-Pd nanoparticles. *J. Am. Chem. Soc.* **2020**, *142* (44), 18971–18980.

(19) Greer, A. L. Metallic glasses on the threshold. *Mater. Today* **2009**, *12* (1), 14–22.

(20) Li, J. Y.; Doubek, G.; McMillon-Brown, L.; Taylor, A. D. Recent advances in metallic glass nanostructures: Synthesis strategies and electrocatalytic applications. *Adv. Mater.* **2019**, *31* (7), 1802120.

(21) Hu, Y. C.; Wang, Y. Z.; Su, R.; Cao, C. R.; Li, F.; Sun, C. W.; Yang, Y.; Guan, P. F.; Ding, D. W.; Wang, Z. L.; Wang, W. H. A highly efficient and self-stabilizing metallic-glass catalyst for electrochemical hydrogen generation. *Adv. Mater.* **2016**, *28* (46), 10293–10297.

(22) Carmo, M.; Sekol, R. C.; Ding, S. Y.; Kumar, G.; Schroers, J.; Taylor, A. D. Bulk metallic glass nanowire architecture for electrochemical applications. *ACS Nano* **2011**, *5* (4), 2979–2983.

(23) Gao, F.-Y.; Liu, S.-N.; Ge, J.-C.; Zhang, X.-L.; Zhu, L.; Zheng, Y.-R.; Duan, Y.; Qin, S.; Dong, W.; Yu, X.; Bao, R.-C.; Yang, P.-P.; Niu, Z.-Z.; Ding, Z.-G.; Liu, W.; Lan, S.; Gao, M.-R.; Yan, Y.; Yu, S.-H. Nickel–molybdenum–niobium metallic glass for efficient hydrogen oxidation in hydroxide exchange membrane fuel cells. *Nat. Catal.* **2022**, *5* (11), 993–1005.

(24) Glasscott, M. W.; Pendergast, A. D.; Goines, S.; Bishop, A. R.; Hoang, A. T.; Renault, C.; Dick, J. E. Electrosynthesis of high-entropy metallic glass nanoparticles for designer, multi-functional electrocatalysis. *Nat. Commun.* **2019**, *10* (1), 2650.

(25) Deng, B.; Meng, W.; Advincula, P. A.; Eddy, L.; Ucak-Astarlioglu, M. G.; Wyss, K. M.; Chen, W.; Carter, R. A.; Li, G.; Cheng, Y.; Nagarajaiah, S.; Tour, J. M. Heavy metal removal from coal fly ash for low carbon footprint cement. *Commun. Eng.* **2023**, *2* (1), 13.

(26) Yan, B.; Krishnamurthy, D.; Hendon, C. H.; Deshpande, S.; Surendranath, Y.; Viswanathan, V. Surface restructuring of nickel sulfide generates optimally coordinated active sites for oxygen reduction catalysis. *Joule* **2017**, *1* (3), 600–612.

(27) Zhang, X.; Luo, Z.; Yu, P.; Cai, Y.; Du, Y.; Wu, D.; Gao, S.; Tan, C.; Li, Z.; Ren, M.; Osipowicz, T.; Chen, S.; Jiang, Z.; Li, J.; Huang, Y.; Yang, J.; Chen, Y.; Ang, C. Y.; Zhao, Y.; Wang, P.; Song, L.; Wu, X.; Liu, Z.; Borgna, A.; Zhang, H. Lithiation-induced

amorphization of Pd3P2S8 for highly efficient hydrogen evolution. *Nat. Catal.* **2018**, *1* (6), 460–468.

(28) He, Y.; Liu, L.; Zhu, C.; Guo, S.; Golani, P.; Koo, B.; Tang, P.; Zhao, Z.; Xu, M.; Zhu, C.; Yu, P.; Zhou, X.; Gao, C.; Wang, X.; Shi, Z.; Zheng, L.; Yang, J.; Shin, B.; Arbiol, J.; Duan, H.; Du, Y.; Heggen, M.; Dunin-Borkowski, R. E.; Guo, W.; Wang, Q. J.; Zhang, Z.; Liu, Z. Amorphizing noble metal chalcogenide catalysts at the single-layer limit towards hydrogen production. *Nat. Catal.* **2022**, *5* (3), 212–221.

(29) Pang, Y.; Zhu, S.; Cui, Z.; Liang, Y.; Li, Z.; Wu, S. Self-supported amorphous nanoporous nickel-cobalt phosphide catalyst for hydrogen evolution reaction. *Prog. Nat. Sci.: Mater. Int.* **2021**, *31* (2), 201–206.

(30) Ma, Y.; Wang, H.; Lv, W.; Ji, S.; Pollet, B. G.; Li, S.; Wang, R. Amorphous PtNiP particle networks of different particle sizes for the electro-oxidation of hydrazine. *RSC Adv.* **2015**, *5* (84), 68655–68661.

(31) Kiani, M. T.; Barr, C. M.; Xu, S. C.; Doan, D.; Wang, Z. X.; Parakh, A.; Hattar, K.; Gu, X. W. Ductile metallic glass nanoparticles via colloidal synthesis. *Nano Lett.* **2020**, *20* (9), 6481–6487.

(32) Zhao, M.; Abe, K.; Yamaura, S.; Yamamoto, Y.; Asao, N. Fabrication of Pd-Ni-P metallic glass nanoparticles and their application as highly durable catalysts in methanol electro-oxidation. *Chem. Mater.* **2014**, *26* (2), 1056–1061.

(33) Wang, W.; He, T.; Yang, X.; Liu, Y.; Wang, C.; Li, J.; Xiao, A.; Zhang, K.; Shi, X.; Jin, M. General synthesis of amorphous PdM (M = Cu, Fe, Co, Ni) alloy nanowires for boosting HCOOH dehydrogenation. *Nano Lett.* **2021**, *21* (8), 3458–3464.

(34) Glasscott, M. W.; Pendergast, A. D.; Goines, S.; Bishop, A. R.; Hoang, A. T.; Renault, C.; Dick, J. E. Electrosynthesis of high-entropy metallic glass nanoparticles for designer, multi-functional electro-catalysis. *Nat. Commun.* **2019**, *10*, 2650.

(35) Zeeshan, M. A.; Esque-de los Ojos, D.; Castro-Hartmann, P.; Guerrero, M.; Nogues, J.; Surinach, S.; Baro, M. D.; Nelson, B. J.; Pane, S.; Pellicer, E.; Sort, J. Electrochemically synthesized amorphous and crystalline nanowires: dissimilar nanomechanical behavior in comparison with homologous flat films. *Nanoscale* **2016**, *8* (3), 1344–1351.

(36) Li, M.-X.; Sun, Y.-T.; Wang, C.; Hu, L.-W.; Sohn, S.; Schroers, J.; Wang, W.-H.; Liu, Y.-H. Data-driven discovery of a universal indicator for metallic glass forming ability. *Nat. Mater.* **2022**, *21* (2), 165–172.

(37) Repa, G. M.; Fredin, L. A. Predicting Electronic Structure of Realistic Amorphous Surfaces. *Adv. Theory Simul.* **2023**, *6* (11), 2300292.

(38) Deng, B.; Wang, Z.; Chen, W.; Li, J. T.; Luong, D. X.; Carter, R. A.; Gao, G.; Yakobson, B. I.; Zhao, Y.; Tour, J. M. Phase controlled synthesis of transition metal carbide nanocrystals by ultrafast flash Joule heating. *Nat. Commun.* **2022**, *13* (1), 262.

(39) Luong, D. X.; Bets, K. V.; Algozeeb, W. A.; Stanford, M. G.; Kittrell, C.; Chen, W.; Salvatierra, R. V.; Ren, M.; McHugh, E. A.; Advincula, P. A.; Wang, Z.; Bhatt, M.; Guo, H.; Mancevski, V.; Shahsavari, R.; Yakobson, B. I.; Tour, J. M. Gram-scale bottom-up flash graphene synthesis. *Nature* **2020**, *577* (7792), 647–651.

(40) Deng, B.; Wang, Z.; Choi, C. H.; Li, G.; Yuan, Z.; Chen, J.; Luong, D. X.; Eddy, L.; Shin, B.; Lathem, A.; Chen, W.; Cheng, Y.; Xu, S.; Liu, Q.; Han, Y.; Yakobson, B. I.; Zhao, Y.; Tour, J. M. Kinetically controlled synthesis of metallic glass nanoparticles with expanded composition space. *Adv. Mater.* **2024**, *36* (15), 2309956.

(41) Deng, B.; Advincula, P. A.; Luong, D. X.; Zhou, J.; Zhang, B.; Wang, Z.; McHugh, E. A.; Chen, J.; Carter, R. A.; Kittrell, C.; Lou, J.; Zhao, Y.; Yakobson, B. I.; Zhao, Y.; Tour, J. M. High-surface-area corundum nanoparticles by resistive hotspot-induced phase trans-formation. *Nat. Commun.* **2022**, *13* (1), 5027.

(42) Green, C. L.; Kucernak, A. Determination of the platinum and ruthenium surface areas in platinum–ruthenium alloy electrocatalysts by underpotential deposition of copper. I. Unsupported catalysts. *J. Phys. Chem. B* **2002**, *106* (5), 1036–1047.

(43) Lee, S. A.; Kim, J.; Kwon, K. C.; Park, S. H.; Jang, H. W. Anion exchange membrane water electrolysis for sustainable large-scale hydrogen production. *Carbon Neutralization* **2022**, *1* (1), 26–48.

(44) Dudarev, S. L.; Botton, G. A.; Savrasov, S. Y.; Humphreys, C. J.; Sutton, A. P. Electron-energy-loss spectra and the structural stability of nickel oxide: An LSDA+U study. *Phys. Rev. B* **1998**, *57* (3), 1505−1509.

(45) Kresse, G.; Furthmuller, J. Efficient iterative schemes for ab initio total-energy calculations using a plane-wave basis set. *Phys. Rev. B* **1996**, *54* (16), 11169−11186.

(46) Blochl, P. E. Projector augmented-wave method. *Phys. Rev. B* **1994**, *50* (24), 17953−17979.

(47) Perdew, J. P.; Wang, Y. Accurate and simple analytic representation of the electron-gas correlation energy. *Phys. Rev. B* **1992**, *45* (23), 13244−13249.

(48) Monkhorst, H. J.; Pack, J. D. Special points for Brillouin-zone integrations. *Phys. Rev. B* **1976**, *13* (12), 5188−5192.

(49) Lechner, W.; Dellago, C. Accurate determination of crystal structures based on averaged local bond order parameters. *J. Chem. Phys.* **2008**, *129* (11), 114707.

(50) Huijbregts, M. A. J.; Steinmann, Z. J. N.; Elshout, P. M. F.; Stam, G.; Verones, F.; Vieira, M.; Zijp, M.; Hollander, A.; van Zelm, R. ReCiPe2016: a harmonised life cycle impact assessment method at midpoint and endpoint level. *Int. J. Life Cycle Assess.* **2017**, *22* (2), 138−147.

(51) Takeuchi, A.; Inoue, A. Quantitative evaluation of critical cooling rate for metallic glasses. *Mater. Sci. Eng., A* **2001**, *304*, 446−451.

(52) Gabski, M.; Peterlechner, M.; Wilde, G. Exploring the phase space of multi-principal-element alloys and predicting the formation of bulk metallic glasses. *Entropy* **2020**, *22* (3), 292.

(53) Butland, A. T. D.; Maddison, R. J. The specific heat of graphite: An evaluation of measurements. *J. Nucl. Mater.* **1973**, *49* (1), 45−56.

(54) Guan, P. F.; Fujita, T.; Hirata, A.; Liu, Y. H.; Chen, M. W. Structural origins of the excellent glass forming ability of Pd40Ni4020. *Phys. Rev. Lett.* **2012**, *108* (17), 175501−175505.

(55) Cheng, L.; Yeung, C. S.; Huang, L.; Ye, G.; Yan, J.; Li, W.; Yiu, C.; Chen, F.-R.; Shen, H.; Tang, B. Z.; Ren, Y.; Yu, X.; Ye, R. Flash healing of laser-induced graphene. *Nat. Commun.* **2024**, *15* (1), 2925.

(56) Romeo, M.; Majerus, J.; Legare, P.; Castellani, N. J.; Leroy, D. B. Photoemission study of Pt adlayers on Ni(111). *Surf. Sci.* **1990**, *238* (1), 163−168.

(57) Riggs, W. M. X-ray photoelectron spectrometry of platinum compounds. *Anal. Chem.* **1972**, *44* (4), 830−832.

(58) Kim, K. S.; Winograd, N.; Davis, R. E. Electron spectroscopy of platinum-oxygen surfaces and application to electrochemical studies. *J. Am. Chem. Soc.* **1971**, *93* (23), 6296−6297.

(59) Jin, Z. L.; Zhang, Y. P. Efficient photocatalytic hydrogen production achieved by WO3 coupled with NiP2 over ZIF-8. *Catal. Surv. Asia* **2020**, *24* (1), 59−69.

(60) Wang, Y. A.; Liu, H. F. Syntheses and characterization of mercapto hydroxyl palladium macromolecular chelates and their catalytic properties. *J. Mol. Catal.* **1988**, *45* (1), 127−142.

(61) Nefedov, V. I.; Salyn, Y. V.; Shtemenko, A. V.; Kotelnikova, A. S. X-ray photoelectron study of trans-influence of the Re-Re multiple bond. *Inorg. Chim. Acta* **1980**, *45*, L49−L50.

(62) Sheng, H. W.; Luo, W. K.; Alamgir, F. M.; Bai, J. M.; Ma, E. Atomic packing and short-to-medium-range order in metallic glasses. *Nature* **2006**, *439* (7075), 419−425.

(63) Dai, J.; Zhu, Y.; Chen, Y.; Wen, X.; Long, M.; Wu, X.; Hu, Z.; Guan, D.; Wang, X.; Zhou, C.; Lin, Q.; Sun, Y.; Weng, S.-C.; Wang, H.; Zhou, W.; Shao, Z. Hydrogen spillover in complex oxide multifunctional sites improves acidic hydrogen evolution electrocatalysis. *Nat. Commun.* **2022**, *13* (1), 1189.

(64) Li, Y.; Peng, C.-K.; Hu, H.; Chen, S.-Y.; Choi, J.-H.; Lin, Y.-G.; Lee, J.-M. Interstitial boron-triggered electron-deficient Os aerogels for enhanced pH-universal hydrogen evolution. *Nat. Commun.* **2022**, *13* (1), 1143.

(65) Tang, J.; Su, C.; Shao, Z. Advanced membrane-based electrode engineering toward efficient and durable water electrolysis and cost-effective seawater electrolysis in membrane electrolyzers. *Exploration* **2024**, *4* (1), 20220112.

(66) Shiva Kumar, S.; Himabindu, V. Hydrogen production by PEM water electrolysis − A review. *Mater. Sci. Energy Technol.* **2019**, *2* (3), 442−454.